In situ mapping of the vectorial electric field within a nanocrystal-based focal plane array using photoemission microscopy

Adrien Khalili, Mariarosa Cavallo, Erwan Bossavit, Rodolphe Alchaar, Tung Huu Dang, Corentin Dabard, Huichen Zhang, Nicolas Ledos, Victor Parahyba, Pierre Potet, et al.

▶ To cite this version:

Adrien Khalili, Mariarosa Cavallo, Erwan Bossavit, Rodolphe Alchaar, Tung Huu Dang, et al.. In situ mapping of the vectorial electric field within a nanocrystal-based focal plane array using photoemission microscopy. ACS Applied Electronic Materials, inPress, 10.1021/acsaelm.3c00609 . hal-04172822

HAL Id: hal-04172822
https://hal.science/hal-04172822v1

Submitted on 28 Jul 2023

In situ mapping of the vectorial electric field within a nanocrystal-based focal plane array using photoemission microscopy

Adrien Khalili[1$], Mariarosa Cavallo[1$], Erwan Bossavit[1,2], Rodolphe Alchaar[1], Tung Huu Dang[1], Corentin Dabard[1], Huichen Zhang[1], Nicolas Ledos[1], Victor Parahyba[3], Pierre Potet[3], James K Utterback[1], Yoann Prado[1], Mathieu G. Silly[2], Pavel Dudin[2], Jose Avila[2], Debora Pierucci[1], Emmanuel Lhuillier[1*]

[1] Sorbonne Université, CNRS, Institut des NanoSciences de Paris, INSP, F-75005 Paris, France.
[2] Synchrotron SOLEIL, L'Orme des Merisiers, Départementale 128, 91190 Saint-Aubin, France.
[3] New Imaging Technologies SA, 1 impasse de la Noisette 91370 Verrières le Buisson, France.

$ these two authors have equal contributions

*To whom correspondence should be sent: el@insp.upmc.fr

Abstract: Within a few years, nanocrystal-based infrared devices have achieved significant progress and advancements, including high-quality imaging systems. This raises the need to develop tools that can probe the device's active material *in situ* and *in operando* to gain a deeper understanding of their operation beyond the overall response of the device. Here, we investigate a short-wave infrared imager based on HgTe nanocrystals with photoconductive operation, which now proposes imaging at wavelengths beyond the traditional InGaAs technology. We demonstrate that we can use photoemission microscopy to probe the energy landscape of this imaging array. Finally, we further use the high spatial resolution of the method to get access to the vectorial distribution of the electric field.

Keywords: infrared, HgTe, imaging, photoemission, microscopy

INTRODUCTION

HgTe nanocrystals[1] (NCs) have emerged as a unique platform to address infrared wavelengths as thanks to the gapless bulk HgTe and bands engineering with quantum confinement. By tailoring the particle surface chemistry, NC arrays can be made conductive and photoconductive.[2–4] As a result, their use in advanced devices dedicated to infrared sensing and imaging appears as a possible alternative to epitaxially grown thin films. Compared with devices relying on narrow band gap epitaxially grown semiconductors, NCs suppress the constraints on epitaxial growth, facilitating coupling to the read-out circuit, including with a few µm pitch circuit.[5] Furthermore, NCs also reduce the amount of toxic material used, now limited to a few hundred nm thick film, while significantly lowering the energy cost relative to the material growth. However, high performance and compatibility with technological developments required by focal plane array (FPA) integration are crucial for the widespread adoption of this technology. Several groups and companies[5–8] have been exploring the use of NCs as an active layer for infrared FPAs relying either on PbS[9,10] or HgTe[11–13] NCs, the latter being the only ones to cover both the short and mid-wave infrared.[14]

To date, technological developments in the field of infrared sensing and imaging have always been linked to progress related to understanding material properties. For instance, in the case of PbS photodiodes, the diode stack was obtained while systematically measuring how surface ligands and associated dipoles shift the energy of the band with respect to the Fermi level. Similar efforts have been made to unveil band alignment[15–17] and complex optical index[18,19] of HgTe NCs to enable a rational design of diode stacks. Nonetheless, prior studies mainly focused on the *non-operando* techniques that ignore the effects of applied electrical field on the diode itself and on the environment, for example, optical spectroscopy, electrochemistry, and conventional photoemission. While such an approach has been satisfying for the design of first-generation devices, it is now essential to consider *in situ* and *under biasing* investigation of the electronic structure. Here, we explore the use of photoemission microscopy as a tool to unveil *operando* the electronic properties of a focal plane array. Recently Cavallo *et al.* have reported the use of such a method to probe the scalar energy landscape of a NC-based field-effect transistor[20,21] and photodiode.[22] In particular, the method has been insightful in probing surface band bending at the NC semiconductor-electrode interface,[20] by providing a direct evidence of the gate bias effect on the band alignment and unveiling the built-in potential of a diode.[23] In this report, we explore how photoemission microscopy can be used to probe the vectorial electric field distribution in a FPA-like structure under operation. Such output will be critical for the future modeling of complex devices such as infrared imagers.

Experimental section

Chemicals: Mercury chloride ($HgCl_2$, Sigma-Aldrich, 99%), **Mercury compounds are highly toxic. Handle them with special care.** Tellurium powder (Te, Sigma-Aldrich, 99.99%), trioctylphosphine (TOP, Alfa Aesar, 90%), oleylamine (OLA, Acros, 80-90%), dodecanethiol (DDT, Sigma-Aldrich, 98%), acetone (VWR), isopropanol (IPA, VWR), ethanol absolute anhydrous (EtOH, VWR), methanol (VWR, >98%), hexane (VWR, 99%), 2-mercaptoethanol (MPOH, Merck, >99%), N,N dimethylformamide (DMF, VWR), toluene (VWR, 99.8%), methylisobutylketone (MIBK, VWR, >98.5%). All chemicals are used without further purification except oleylamine that is centrifuged before use.

1 M TOP:Te: 2.54 g of Te powder are mixed in 20 mL of TOP in a three neck flask. The flask is kept under vacuum at room temperature for 5 min and then the temperature is raised to 100 °C.

Furthermore, degassing of flask is conducted for the next 20 min. The atmosphere is switched to nitrogen and the temperature is raised to 275 °C. The solution is stirred until a clear orange coloration is obtained. The flask is cooled down to room temperature and the color change to yellow. Finally, this solution is transferred to a nitrogen filled glove box for storage.

HgTe NCs synthesis with band-edge at 6000 cm^{-1}: In a 250 mL three neck flask, 1360 mg of $HgCl_2$ (5 mmol) and 125 mL of oleylamine are degassed under vacuum at 110 °C. Meanwhile 5 mL of TOP:Te (1 M) are extracted from glove box and mixed with 5 mL of oleylamine. After the atmosphere is switched to N_2 and the temperature stabilized at 56 °C, the TOP:Te solution is quickly injected. After 3 min, 10 mL of a mixture of DDT in toluene (25% of DDT) are injected and a water bath is used to quickly decrease the temperature. The content of the flask is split over 7 centrifugation tubes (50 mL) and MeOH is added (up to 40 mL). After centrifugation the formed pellet is redispersed in two centrifugation tubes with toluene. The solution is precipitated a second time with absolute EtOH (up to 40 mL). Again, the formed pellet is redispersed in toluene. At this step the nanocrystals are centrifuged in pure toluene to get rid of the lamellar phase. The solid phase is discarded. The stable phase is transferred in a vial after filtration (0.22 µm) with a volume of toluene V = 16 mL.

HgTe ink: 3 mL of the CQD solution in toluene (0.9 OD at 400 nm after a 500x dilution) is mixed with 1.2 mL of exchange solution (15 mg $HgCl_2$, 9 mL DMF, 1 mL MPOH) and 0.8 mL of DMF. The solution is vortexed and sonicated for 3 min to help the ligand exchange. Then, the solution is precipitated by adding toluene and centrifuged at 6000 rpm for 3 min. The supernatant is discarded and the QDs are dried under vacuum. Finally, the NCs are redispersed in 250 µL of DMF, centrifuged for 2 min at 6000 rpm and filtered through a 0.22 µm PTFE filter.

Material characterization: For TEM imaging, a drop of diluted NCs solution is casted on a copper grid covered with an amorphous carbon film. The grid is degassed overnight under secondary vacuum. A JEOL 2010F is used at 200 kV for the acquisition of pictures.
For infrared spectroscopy, we use a Fischer Nicolet iS50 in attenuated total reflection (ATR) mode. The source is a white halogen lamp, the beamsplitter made of CaF_2 and the detector is a DTGS ATR. Spectra are typically acquired between 10 000 and 2100 cm^{-1} with a 4 cm^{-1} resolution and averaged over 32 spectra.

Photoemission microscopy: The spatially resolved photoemission maps were measured at the ANTARES beamline of Synchrotron SOLEIL. We used linearly horizontal polarized photons with a photon energy of 95 eV and MBS A-1 hemispherical electron analyzer.[24] All measurements were conducted at 250 K, with an energy resolution better than 30 meV and a spatial resolution as low as 700 nm along the pn junction (indicated as X-direction in all figures). For all maps, angular dispersion of the analyzer (±15°) is neglected by integrating the spectra over all angles. The samples were mounted on the *in operando* sample holder of ANTARES beamline and directly grounded to it via silver paste. The sample holder was then grounded through the manipulator. The acquired data were processed using Wavemetrics Igor Pro. In particular, the binding energy maps were obtained by fitting a double gaussian to the measured spectra point-by-point and then plotting the binding energy value of the Hg $5d_{5/2}$ contribution. To evaluate the energy shift, the photoemission spectra were averaged over a small number of points (5 or 10) in the regions of interest. Binding energy calibration was performed by measuring the Fermi edge of a gold substrate mounted on the same sample holder of the device.

High-resolution photoemission spectroscopy: To characterize the HgTe NC band alignment, additional non-spatially resolved measurements were performed at Tempo beamline[25] of synchrotron Soleil. Films of NCs were spin-cast onto a Si substrate coated with 80 nm of gold. The ligands of the NCs were exchanged using the same procedure as for device fabrication to avoid any charging effects during measurements. The samples were introduced in the preparation chamber and degassed under a vacuum below 10^{-9} mbar for at least two hours. Then the samples were introduced into the analysis chamber. The signal was acquired with an MBS A-1 photoelectron analyzer. The acquisition was done at a constant pass energy (50 eV) within the detector. A photon energy of 150 eV was used for the acquisition of valence band and work function while a 600 eV photon energy was used for the analysis of the core levels. A gold substrate was used to calibrate the Fermi energy. The absolute value of the incoming photon energy was determined by measuring the second order of Au 4f core level peaks. Then for a given analyzer pass energy, we measured the Fermi edge and set its binding energy as zero. The same shift was applied to all spectra acquired with the same pass energy. To determine the work function, we applied 18 V bias, whose exact value was determined by looking at the shift of a Fermi edge.

RESULTS AND DISCUSSION

To motivate our work related to *in situ* investigation of device energy landscape, we start by designing a short-wave infrared (SWIR) imager with the active layer of HgTe NCs. The latter are grown using the Keuleyan's procedure[26] in which mercury chloride is reacted with trioctylphosphine telluride in oleylamine used as coordinating solvent. To obtain SWIR absorbing NCs, the reaction is conducted at low temperature (56°C) and for a short duration (3 min). The obtained NCs are branched particles as shown on the transmission electron microscopy image, see **Figure 1**a. As grown, they present an excitonic feature at around 1.5 µm, see **Figure 1**b. After conducting a ligand exchange step, the absorption spectrum is further redshifted, bringing the excitonic peak to 1.8 µm, with a cut-off wavelength at 2 µm, see Figure S3-S4. The resulting material is capped[27,28] with a mixture of $HgCl_2$ and short thiols and presents a *p*-type conduction (**Figure 1**c) consistent with its electronic structure as discussed later.

To build a focal plane array, the ink of HgTe NCs has to be coupled to a read-out circuit. Here, we use the video graphics array (VGA: 640x512 pixels) format circuit (model 1601 Quantum c from New Imaging Technologies), featuring a 15 µm pixel size, see a schematic in **Figure 1**d. This circuit, in particular, enables the application of a checkerboard electric field bias of two consecutive pixels. This in-plane application of the electric field enables the photoconductive operation of the NC film. Consequently, imaging can be achieved by depositing a single layer rather than stacking multiple layers, like in photodiode-based imagers. This simplifies the fabrication by reducing the number of steps, and results in the higher-quality homogeneous film (Figure S1). Example images captured using this sensor are presented in **Figure 1**e and f. The quality of the image stresses the high quality of the thin film deposition, with neither coffee ring effects nor large areas of dead pixels.

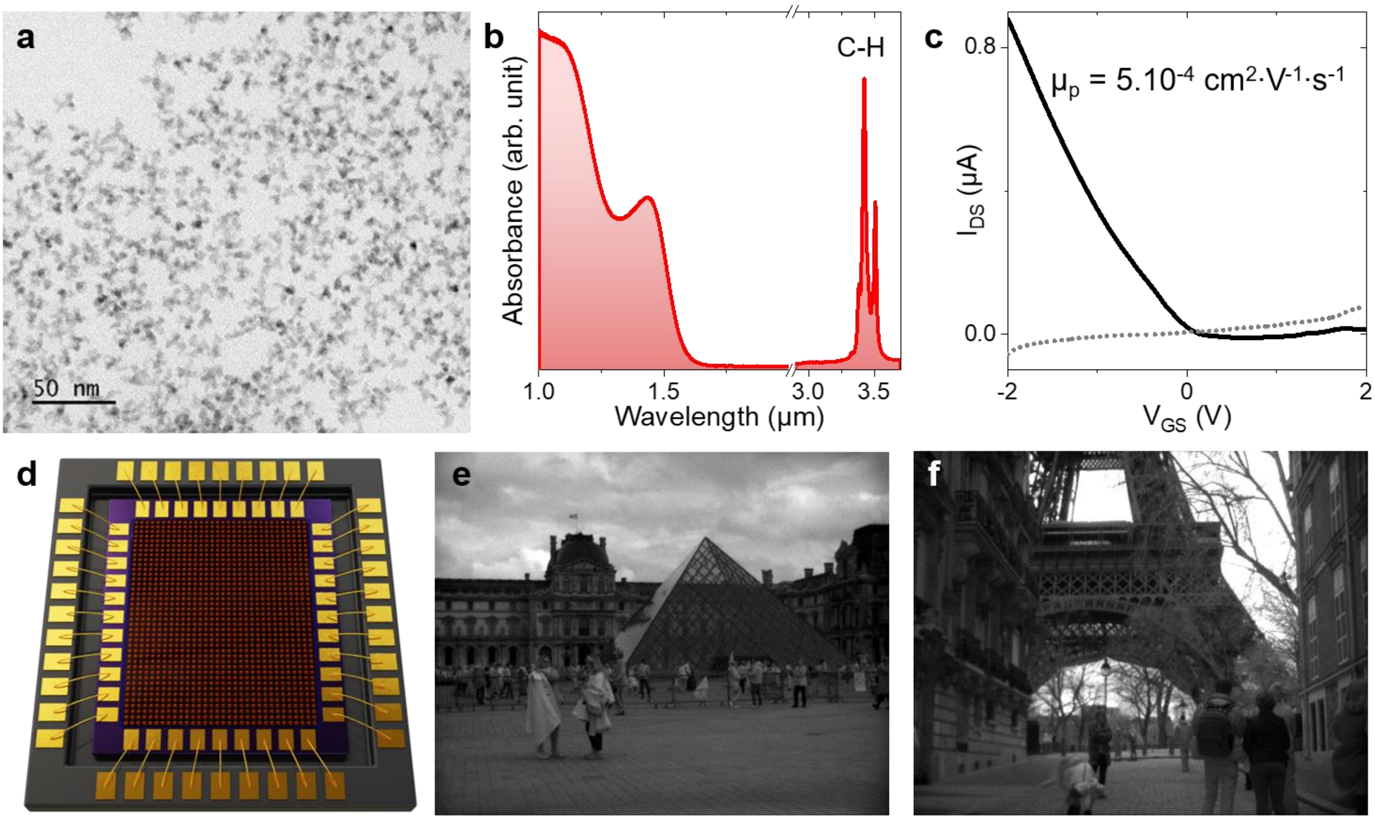

***Figure 1 HgTe nanocrystals for short-wave infrared imaging**. a. TEM image of the HgTe NCs used for SWIR imaging. b. Infrared absorption spectrum of the HgTe NCs after synthesis. c. Transfer curve (i.e., drain (solid black) and gate (dashed grey current as a function of the applied gate bias under constant 100 mV drain source bias) for HgTe NC film as used for imaging. d. Schematic of the HgTe NC film deposited onto a VGA format Read-Out Integrated Circuit (ROIC) with photoconductive operation. e. Image of the Louvre Museum in Paris acquired with the camera based on HgTe NCs. f. Image of the Eiffel tower in Paris acquired with the camera based on HgTe NCs.*

In order to conduct photoemission microscopy measurements, we developed a sample that mimics the ROIC. The sample is made of 8 pixels with a similar spacing (15 µm) and geometrical factors as those used within the ROIC (Read Out Integrated Circuit), see **Figure 2**a and S2 for the fabrication procedure. It enables full control over the bias distribution. Contact lines are buried below a silica layer to prevent them from being part of the photocharge collection. Thus, only the tips of the electrodes are electrically active, similar to the case of the actual ROIC. This focal plane array-like device is then characterized in terms of performance for SWIR sensing. The dark current has been measured under various temperatures down to 150 K, see **Figure 2**b. The current density under 2 V operation at 250 K is around 500 µA.cm^{-2}. The current is decreased by two orders of magnitude as the sample is cooled down from room temperature to 200 K corresponding to a 260 meV activation energy, see **Figure 2**c. This is slightly smaller than the characteristic value of half the band gap (E_G/2=350 meV) when the balance between generation and recombination is the main mechanism defining the carrier density.

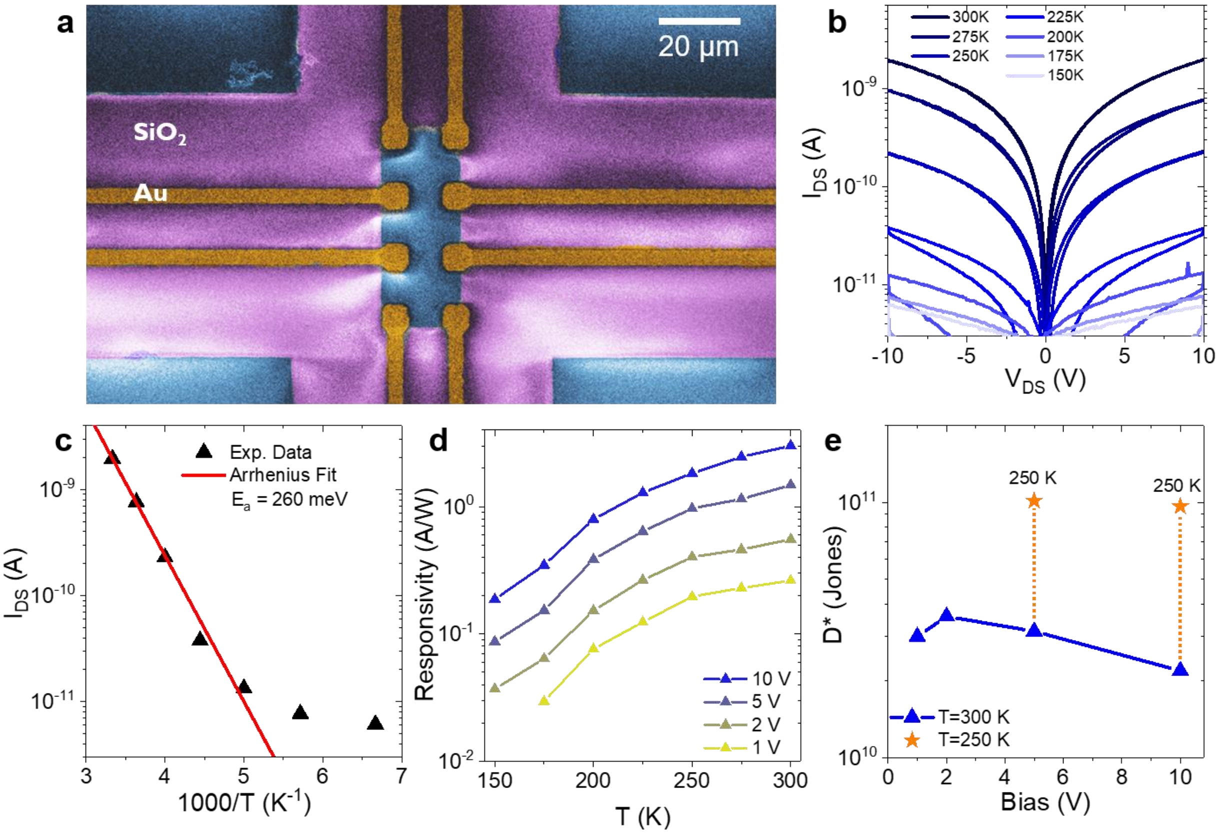

***Figure 2 Focal plane array-like structure and performances for SWIR detection**. a. False-colored optical microcopy image of the focal plane array-like structure with 15 µm pixel pitch. Substrate is blue, silica appears purple and gold contact are goldy. b. IV curves from the device depicted in part a at various temperatures. Darker curves correspond to higher temperatures. c. Current as a function of the temperature (scatter) and its Arrhenius fit (red line). d. Responsivity as function of the temperature under various applied biases. e. Detectivity as function of the applied bias at room temperature and at 250 K.*

Figure 2d shows the device's responsivity under broadband blackbody (T=980°C) illumination. In this range of bias and temperature, higher responsivities are obtained under a larger electric field or while increasing the operating temperature. Responsivity relates to the external quantum efficiency (EQE) through the simple expression $R = \frac{\mathrm{EQE}\cdot e}{h\nu}$, with e the proton charge and $h\nu$ the incident photon energy. A responsivity value above ≈2 $A\cdot W^{-1}$ corresponds to EQE above 100 % which is the signature of photogain in this system.[29–31] FET measurements (**Figure 1**c) have shown a p-type behavior for the material, that may seem surprising given the fact that the hole effective mass in HgTe is 25 times heavier than the electron,[32] prompting further clarification. Under illumination, photo-holes provide the charge transport while electrons with their reduced mobility behave almost as trapped. Once the hole reaches the electrode, it will be reinjected in the film by the opposite electrode to ensure the electroneutrality of the sample. This process lasts until the slow electron recombines. This mechanism generates several holes per absorbed photon and it is responsible for the rather large photoresponse observed in our device. The noise appears to be *1/f* dominated (Figure S8), as expected for a photoconductive NC-based device.[33,34] The resulting detectivity value at room temperature is maximized when a potential of 2 V is applied and reaches 4×10^{10} Jones. The detectivity reaches 10^{11} Jones at 250 K, see **Figure 2**e.

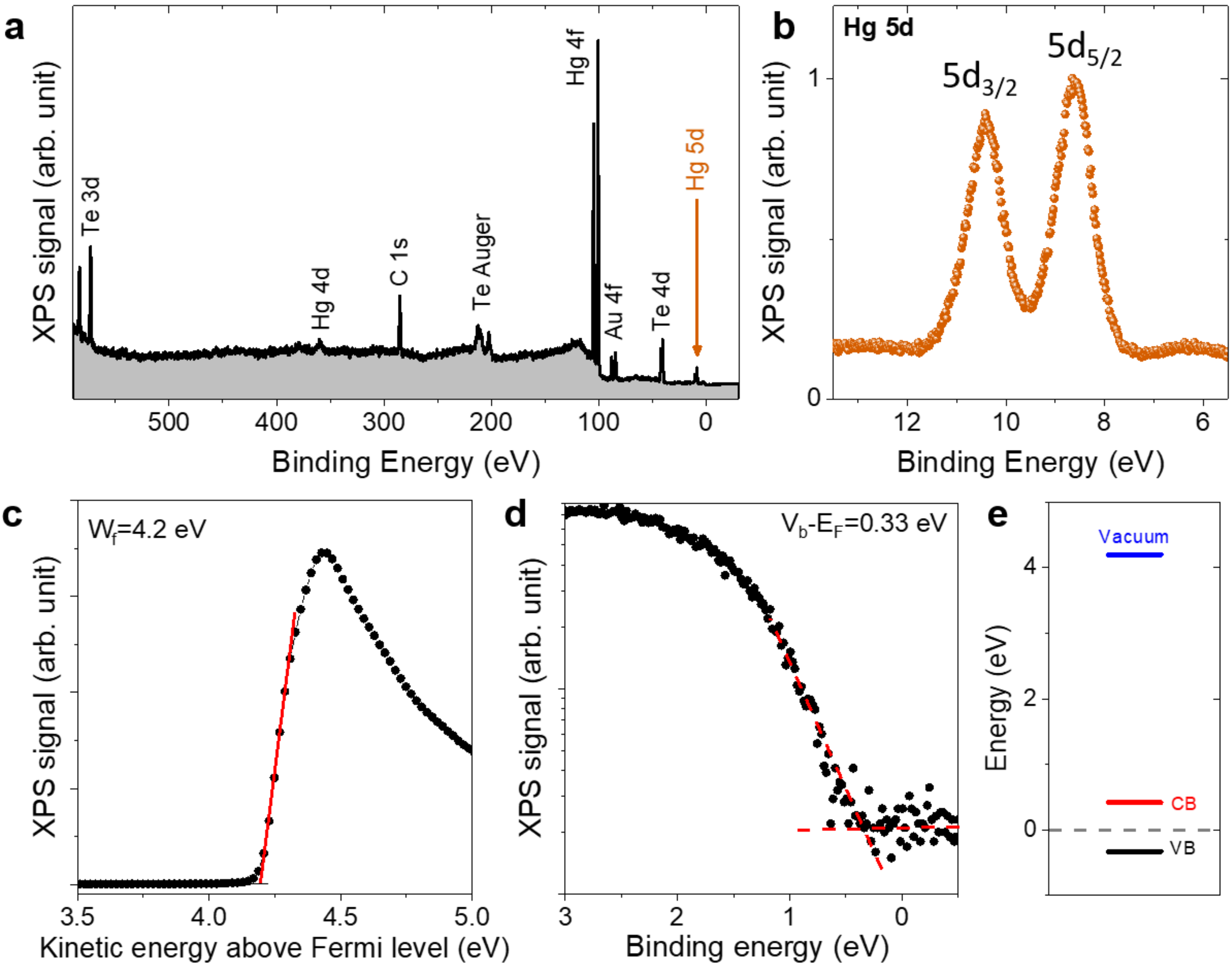

Figure 3 X-ray photoemission spectroscopy of HgTe NC thin film. *a. Overview spectrum acquired at hv=700 eV. Contribution from gold is due to its presence in the substrate (used to prevent sample charging). b. X-ray photoemission spectrum of the Hg 5d state. c. X-ray photoemission spectrum of the secondary electron cut-off. d. X-ray photoemission spectrum of the valence band. e. Reconstructed electronic spectrum of the HgTe NC used in device assuming an optical band gap of 0.7 eV.*

To prepare the photoemission microscopy study, conventional (i.e., non-spatially resolved) X-ray photoemission spectroscopy on the active layer used in the focal plane array-like structure is carried out first. **Figure 3**a shows the photoemission survey spectrum. the same film preparation is performed to ensure that the NC film is representative of the device. Beyond being similar to the actual film, enhancing the film conductivity reduces the possibility of sample charging, which may lead to electrostatic shifts of the core level states. The survey spectrum presents contributions from Hg and Te. A small contribution of the Au 4f state is attributed to the gold used as the substrate to reduce charging effects further. We also observe a small contribution of carbon attributed to the mercaptoethanol ligands. Peaks relative to S and Cl have a weak cross section or come with very low amount and are thus not observed. It is also worth pointing out that we do not notice any contribution from oxygen despite the film was prepared under air condition. This observation is consistent with the recent report by Zhang *et al.* that concluded with the weak propensity of HgTe NCs for oxidation.[12] This lack of oxidation will leave the state close to the valence band free from oxide contribution, which is critical for photoemission microscopy. X-ray beam focusing is accomplished by introducing a Fresnel zone plate over the synchrotron beam, which focuses the beam from conventional level of 100 µm down to 700 nm. Compared with transmission electron microscopy technique such as 4D STEM[35,36] which also have been used to unveil vectorial mapping of electric field of device, photoemission microscopy has certainly a reduced resolution, but also requires minimal constrain in device update.

Here, we can rely on the Hg 5d state that presents a binding energy at around 8.5 eV, see **Figure 3**b. We also investigate the valence band state and reveal that the latter is 0.3 eV below the Fermi level, see **Figure 3**d and e. Firstly, this locates the Fermi level in the bottom part of the band gap, explaining why *p* conduction is observed. Secondly, we can connect this value to the thermal activation energy, which can be attributed to the thermal activation of the hole. Although the material is not exactly intrinsic, the Fermi level is still quite deep in the band gap, explaining also why this material is relevant for photodetection. Finally, by measuring the low energy cut-off of the secondary electrons, we can determine the material work function (≈4.2 eV) and propose a reconstructed energy diagram in absolute energy scale, see **Figure 3**e.

In the last part of this work, we aim to use soft X-ray photoemission microscopy to unveil the vectorial distribution of the applied electric field. As pointed out, a synchrotron beam is first focused and used to illuminate the sample with 700 nm resolution. The sample is raster-scanned in front of an electron analyzer, and a photoemission spectrum is collected for each point. The collected data forms a 3D matrix of the photoemission intensity as a function of kinetic energy and (X;Y) position in the sample plane. Then, for each point, we fit with a double gaussian shape curve the photoemission spectrum of the Hg 5d state with the Voigt function to extract its binding energy. A schematic of the experiment is given in **Figure 4**a. As already pointed-out in previous work,[20] the method is relevant to track the bias drop, see **Figure 4**b. The bias drop between two pixels appears almost linear (*i.e.,* constant electric field), which is the expected distribution for a diffusive transport mechanism as it is in nanocrystalline materials, where conduction occurs through hopping.[37,38] This situation contrasts with a bias drop that would be accumulated near the edge contact if ballistic transport occurred. However, in this focal plane array-like structure, the 1D plot of the energy drop hides the distribution of the electric field vector ($\vec{F}$). In a previous study where a field-effect transistor was in focus, the author employed a quasi-infinite geometry along one direction, making the electric field mostly 1D. Here, the geometry of the device favors a radial distribution of the electric field around a pixel. The high-resolution mapping of the energy landscape enables the extraction of the energy landscape gradient. As $\vec{F} = -\nabla V$, where V is the electric potential, one can directly relate the experimental data through $\vec{F} = +\nabla KE = \frac{\partial KE}{\partial x}\hat{x} + \frac{\partial KE}{\partial y}\hat{y}$**,** where KE is the measured kinetic energy profile. The electric field mapping between two pixels is shown in **Figure 4**c. As expected, the electric potential V above the metallic electrodes is constant (equipotential), resulting in a null electric field (≈ 0). However, one can notice that the electric field is not limited to the area between the pixels and that transport will occur over a larger area.

To further understand the experimental distribution of the electric field, we have conducted electrostatic simulation. In Figure S6, we have used the nominal structure, where the electrodes exhibit a square shape and HgTe is only between the electrodes. Though the overall electrostatic field is close to its average value, a clear tip effect is revealed at the metal semiconductor interface and especially at the corner of the electrodes. This situation contrasts with the experimental result where the field is null on the top of the electrode and gradually increases from the vicinity of the electrode, reaching a maximum in the middle region between the electrodes. To suppress this tip effect, we have to consider a smoother shape of the electrode with smooth edges and rounded corners. Additionally, it is essential to account for the fact that the probed field is obtained within the HgTe film and not in air, see Figure S7. In this case, the tip effect is suppressed and we observe, consistent with the experimental observations, a rise of the electric field from the electrodes.

In the region of interest within the structure (i.e., in the center), where the electric field is experimentally observed to reach its maximum, its value is measured to be 1.2 kV.cm^{-1}. The latter closely aligns with the average value obtained from the ratio of the applied bias over the distance between electrodes. However, the distribution of the electrostatic film magnitude (Figure S8) appears significantly broad. The presence of such a broad distribution poses additional challenges in transport modelling, as the diffusion length is also influenced by the magnitude of the electric field.[39–43] Nevertheless, a higher field away from the electrode will ease the charge collection, compared to the situation where the field is more homogeneous and where charge collection in the vicinity of the electrode is favored.

This type of tool will thus be relevant to better define the actually optically active area of device, which is an important parameter to quantify device performances. It would be attractive to couple the tools enabling electronic structure investigation with scanning near-field optical microscopy (SNOM) mapping of the electromagnetic field and local mapping of the photocurrent.

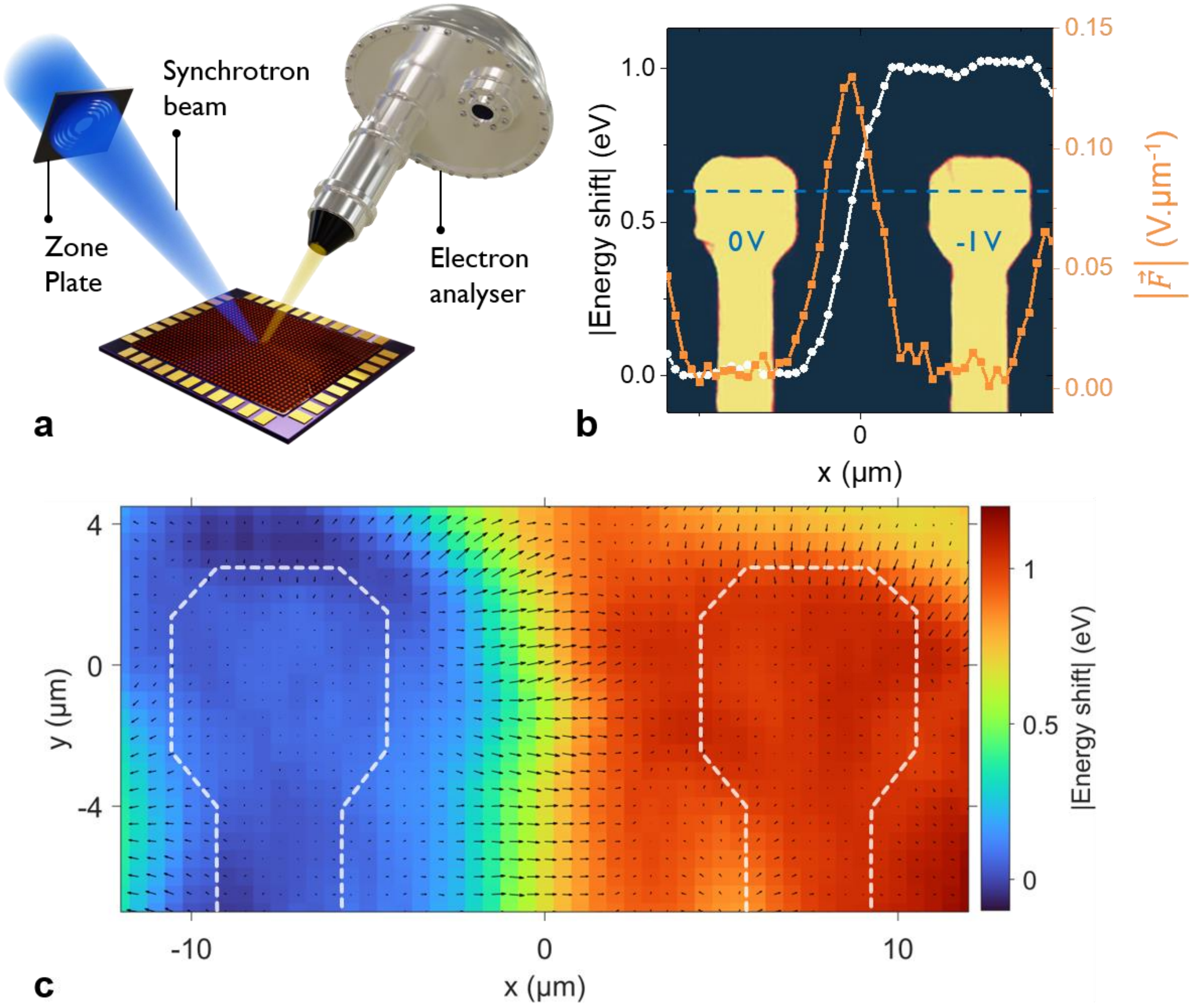

Figure 4 X-ray photoemission microscopy applied to a focal plane array-like device. *a. Schematic of the photoemission microscopy setup. b. Energy shift for the Hg 5d state (white line) across the area between two pixels (blue dashed line) as 1 V is applied over them. The profile is obtained by subtracting the profile with grounded electrodes. The orange plot corresponds to the electric field value across the area between two pixels (blue dashed line). A microscopy image of the device is added as background. c. Energy shift mapping (color map) for the Hg 5d state over the area between two pixels as 1 V is applied between them. On top of it, an arrow map indicating the direction and modulus of the electric field as obtained from the gradient of the kinetic energy map.*

CONCLUSION

Integrating nanocrystals into advanced devices requires the development of experimental tools that are able to unveil the material properties in a realistic dielectric environment under operation. Here, we focus on SWIR focal plane arrays which use an active layer made of HgTe NCs. These devices provide high-quality imaging capabilities and meet the detection level requirements of field application. We demonstrate that scanning photoemission microscopy is a relevant tool not only to probe the energy landscape of the device under biasing but also to unveil the vectorial distribution of the electric field, which cannot be described by a scalar quantity in this device. The method appears very general since it has been applied to various device geometry, including field-effect transistors, diodes, and now focal-plane arrays. The next step is integrating the 2D mapping results with simulation tools and developing phototransport nanoprobe techniques to establish a correlation between the static energy landscape and conduction at the mesoscopic scale.

SUPPORTING INFORMATION

Supporting Information include details about (i) device fabrication, (ii) device optoelectronic characterization and (iii) electrostatic simulation of the electric field map.

ACKNOWLEDEGMENTS

The project is supported by ERC grants blackQD (grant n° 756225), and AQDtive (grant n°101086358). This work was supported by French state funds managed by the Agence Nationale de la recherche (ANR) through the grant IPER-Nano2 (ANR-18CE30-0023-01), Copin (ANR-19-CE24-0022), Frontal (ANR-19-CE09-0017), Graskop (ANR-19-CE09-0026), NITQuantum (ANR-20-ASTR-0008), Bright (ANR-21-CE24-0012), MixDFerro (ANR-21-CE09-0029), Quicktera (ANR-22-CE09-0018) and Operatwist (ANR-22-CE09-0037-01). This project has received financial support from the CNRS through the MITI interdisciplinary programs (project within).

CONFLICT OF INTEREST

The authors declare no competing interest.

Data availability

The data that support the findings of this study are available from the corresponding author upon reasonable request.

REFERENCES

(1) Gréboval, C.; Chu, A.; Goubet, N.; Livache, C.; Ithurria, S.; Lhuillier, E. Mercury Chalcogenide Quantum Dots: Material Perspective for Device Integration. *Chem. Rev.* **2021**, *121* (7), 3627–3700.

(2) Tian, Y.; Luo, H.; Chen, M.; Li, C.; Kershaw, S. V.; Zhang, R.; Rogach, A. L. Mercury Chalcogenide Colloidal Quantum Dots for Infrared Photodetection: From Synthesis to Device Applications. *Nanoscale* **2023**, *15* (14), 6476–6504.

(3) Zhao, X.; Mu, G.; Tang, X.; Chen, M. Mid-IR Intraband Photodetectors with Colloidal Quantum Dots. *Coatings* **2022**, *12* (4), 467.

(4) Nakotte, T.; Munyan, S. G.; Murphy, J. W.; Hawks, S. A.; Kang, S.; Han, J.; Hiszpanski, A. M. Colloidal Quantum Dot Based Mid-Infrared Detectors: Moving from Single Pixel Devices in the Lab to Cameras in the Field. *Journal of Materials Chemistry C* **2021**, *10* (LLNL-JRNL-828879).

(5) Steckel, J. S.; Josse, E.; Pattantyus-Abraham, A. G.; Bidaud, M.; Mortini, B.; Bilgen, H.; Arnaud, O.; Allegret-Maret, S.; Saguin, F.; Mazet, L.; Lhostis, S.; Berger, T.; Haxaire, K.; Chapelon, L. L.; Parmigiani, L.; Gouraud, P.; Brihoum, M.; Bar, P.; Guillermet, M.; Favreau, S.; Duru, R.; Fantuz, J.; Ricq, S.; Ney, D.; Hammad, I.; Roy, D.; Arnaud, A.; Vianne, B.; Nayak, G.; Virollet, N.; Farys, V.; Malinge, P.; Tournier, A.; Lalanne, F.; Crocherie, A.; Galvier, J.; Rabary, S.; Noblanc, O.; Wehbe-Alause, H.; Acharya, S.; Singh, A.; Meitzner, J.; Aher, D.; Yang, H.;

Romero, J.; Chen, B.; Hsu, C.; Cheng, K. C.; Chang, Y.; Sarmiento, M.; Grange, C.; Mazaleyrat, E.; Rochereau, K. 1.62 µm Global Shutter Quantum Dot Image Sensor Optimized for Near and Shortwave Infrared. In *2021 IEEE International Electron Devices Meeting (IEDM)*; 2021; p 23.4.1-23.4.4.

(6) *Emberion*. Emberion. https://www.emberion.com/ (accessed 2023-03-28).

(7) *SWIR Vison Systems*. https://www.swirvisionsystems.com/ (accessed 2023-03-28).

(8) Pejović, V.; Georgitzikis, E.; Lee, J.; Lieberman, I.; Cheyns, D.; Heremans, P.; Malinowski, P. E. Infrared Colloidal Quantum Dot Image Sensors. *IEEE Transactions on Electron Devices* **2022**, *69* (6), 2840–2850.

(9) Liu, J.; Liu, P.; Chen, D.; Shi, T.; Qu, X.; Chen, L.; Wu, T.; Ke, J.; Xiong, K.; Li, M.; Song, H.; Wei, W.; Cao, J.; Zhang, J.; Gao, L.; Tang, J. A Near-Infrared Colloidal Quantum Dot Imager with Monolithically Integrated Readout Circuitry. *Nat Electron* **2022**, *5* (7), 443–451.

(10) Malinowski, P. E.; Pejović, V.; Lieberman, I.; Kim, J. H.; Siddik, A. B.; Georgitzikis, E.; Lim, M. J.; Hagelsieb, L. M.; Hermans, Y.; Monroy, I. P.; Song, W.; Basak, S.; Gehlhaar, R.; Roose, F. D.; Siskos, A.; Papadopoulos, N.; Thijs, S.; Vershooten, T.; Chandrasekaran, N.; Li, Y.; Soussan, P.; Genoe, J.; Heremans, P.; Lee, J.; Cheyns, D. Image Sensors Using Thin-Film Absorbers. *Appl. Opt., AO* **2023**, *62* (17), F21–F30.

(11) Gréboval, C.; Darson, D.; Parahyba, V.; Alchaar, R.; Abadie, C.; Noguier, V.; Ferré, S.; Izquierdo, E.; Khalili, A.; Prado, Y.; Potet, P.; Lhuillier, E. Photoconductive Focal Plane Array Based on HgTe Quantum Dots for Fast and Cost-Effective Short-Wave Infrared Imaging. *Nanoscale* **2022**, *14* (26), 9359–9368.

(12) Zhang, H.; Alchaar, R.; Prado, Y.; Khalili, A.; Gréboval, C.; Cavallo, M.; Bossavit, E.; Dabard, C.; Dang, T. H.; Abadie, C.; Methivier, C.; Darson, D.; Parahyba, V.; Potet, P.; Ramade, J.; Silly, M. G.; Utterback, J. K.; Pierucci, D.; Ithurria, S.; Lhuillier, E. Material Perspective on HgTe Nanocrystal-Based Short-Wave Infrared Focal Plane Arrays. *Chem. Mater.* **2022**, *34* (24), 10964–10972.

(13) Zhang, S.; Bi, C.; Qin, T.; Liu, Y.; Cao, J.; Song, J.; Huo, Y.; Chen, M.; Hao, Q.; Tang, X. Wafer-Scale Fabrication of CMOS-Compatible Trapping-Mode Infrared Imagers with Colloidal Quantum Dots. *ACS Photonics* **2023**, *10* (3), 673–682.

(14) Buurma, C.; Pimpinella, R. E.; Ciani, A. J.; Feldman, J. S.; Grein, C. H.; Guyot-Sionnest, P. MWIR Imaging with Low Cost Colloidal Quantum Dot Films. In *Optical Sensing, Imaging, and Photon Counting: Nanostructured Devices and Applications 2016*; SPIE, 2016; Vol. 9933, p 993303.

(15) Chen, M.; Guyot-Sionnest, P. Reversible Electrochemistry of Mercury Chalcogenide Colloidal Quantum Dot Films. *ACS Nano* **2017**, *11* (4), 4165–4173.

(16) Ruppert, M.; Bui, H.; Sagar, L. K.; Geiregat, P.; Hens, Z.; Bester, G.; Huse, N. Intraband Dynamics of Mid-Infrared HgTe Quantum Dots. *Nanoscale* **2022**, *14* (11), 4123–4130.

(17) Chu, A.; Martinez, B.; Ferré, S.; Noguier, V.; Gréboval, C.; Livache, C.; Qu, J.; Prado, Y.; Casaretto, N.; Goubet, N.; Cruguel, H.; Dudy, L.; Silly, M. G.; Vincent, G.; Lhuillier, E. HgTe Nanocrystals for SWIR Detection and Their Integration up to the Focal Plane Array. *ACS Appl. Mater. Interfaces* **2019**, *11* (36), 33116–33123.

(18) Rastogi, P.; Chu, A.; Dang, T. H.; Prado, Y.; Gréboval, C.; Qu, J.; Dabard, C.; Khalili, A.; Dandeu, E.; Fix, B.; Xu, X. Z.; Ithurria, S.; Vincent, G.; Gallas, B.; Lhuillier, E. Complex Optical Index of HgTe Nanocrystal Infrared Thin Films and Its Use for Short Wave Infrared Photodiode Design. *Advanced Optical Materials* **2021**, *9* (10), 2002066.

(19) Chehaibou, B.; Izquierdo, E.; Chu, A.; Abadie, C.; Cavallo, M.; Khalili, A.; Dang, T. H.; Greboval, C.; Xu, X. Z.; Ithurria, S. The Complex Optical Index of PbS Nanocrystal Thin Films and Their Use for Short Wave Infrared Sensor Design. *Nanoscale* **2022**, *14* (7), 2711–2721.

(20) Cavallo, M.; Bossavit, E.; Zhang, H.; Dabard, C.; Dang, T. H.; Khalili, A.; Abadie, C.; Alchaar, R.; Mastrippolito, D.; Prado, Y.; Becerra, L.; Rosticher, M.; Silly, M. G.; Utterback, J. K.; Ithurria, S.; Avila, J.; Pierucci, D.; Lhuillier, E. Mapping the Energy Landscape from a Nanocrystal-Based

Field Effect Transistor under Operation Using Nanobeam Photoemission Spectroscopy. *Nano Lett.* **2023**, *23* (4), 1363–1370.

(21) Cavallo, M.; Bossavit, E.; Matzen, S.; Maroutian, T.; Alchaar, R.; Dang, T.; Khalili, A.; Dabard, C.; Zhang, H.; Prado, Y.; Abadie, C.; Utterback, J.; Dayen, J.-F.; Silly, M.; Dudin, P.; Ávila, J.; Lhuillier, E.; Pierucci, D. Coupling Ferroelectric to Colloidal Nanocrystals as a Generic Strategy to Engineer the Carrier Density Landscape. *Advanced Functional Materials* **2023,** 2300846.

(22) Cavallo, M.; Alchaar, R.; Bossavit, E.; Zhang, H.; Dang, T. H.; Khalili, A.; Prado, Y.; Silly, M. G.; Utterback, J. K.; Ithurria, S.; Dudin, P.; Avila, J.; Pierucci, D.; Lhuillier, E. Inside a Nanocrystal-Based Photodiode Using Photoemission Microscopy. *Nanoscale* **2023**, *15* (21), 9440–9448.

(23) Cavallo, M.; Alchaar, R.; Bossavit, E.; Zhang, H.; Dang, T. H.; Khalili, A.; Prado, Y.; Silly, M. G.; Utterback, J. K.; Ithurria, S.; Dudin, P.; Avila, J.; Pierucci, D.; Lhuillier, E. Inside a Nanocrystal-Based Photodiode Using Photoemission Microscopy. *Nanoscale* **2023**, 15, 9440-9448.

(24) Avila, J.; Razado-Colambo, I.; Lorcy, S.; Lagarde, B.; Giorgetta, J.-L.; Polack, F.; Asensio, M. C. ANTARES, a Scanning Photoemission Microscopy Beamline at SOLEIL. *J. Phys.: Conf. Ser.* **2013**, *425* (19), 192023.

(25) Polack, F.; Silly, M.; Chauvet, C.; Lagarde, B.; Bergeard, N.; Izquierdo, M.; Chubar, O.; Krizmancic, D.; Ribbens, M.; Duval, J. -P.; Basset, C.; Kubsky, S.; Sirotti, F. TEMPO: A New Insertion Device Beamline at SOLEIL for Time Resolved Photoelectron Spectroscopy Experiments on Solids and Interfaces. *AIP Conference Proceedings* **2010**, *1234* (1), 185–188.

(26) Keuleyan, S.; Lhuillier, E.; Guyot-Sionnest, P. Synthesis of Colloidal HgTe Quantum Dots for Narrow Mid-IR Emission and Detection. *J. Am. Chem. Soc.* **2011**, *133* (41), 16422–16424.

(27) Martinez, B.; Ramade, J.; Livache, C.; Goubet, N.; Chu, A.; Gréboval, C.; Qu, J.; Watkins, W. L.; Becerra, L.; Dandeu, E.; Fave, J. L.; Méthivier, C.; Lacaze, E.; Lhuillier, E. HgTe Nanocrystal Inks for Extended Short-Wave Infrared Detection. *Advanced Optical Materials* **2019**, *7* (15), 1900348.

(28) Lan, X.; Chen, M.; Hudson, M. H.; Kamysbayev, V.; Wang, Y.; Guyot-Sionnest, P.; Talapin, D. V. Quantum Dot Solids Showing State-Resolved Band-like Transport. *Nat. Mater.* **2020**, *19* (3), 323–329.

(29) Zhang, S.; Bi, C.; Qin, T.; Liu, Y.; Cao, J.; Song, J.; Huo, Y.; Chen, M.; Hao, Q.; Tang, X. Wafer-Scale Fabrication of CMOS-Compatible Trapping-Mode Infrared Imagers with Colloidal Quantum Dots. *ACS Photonics* **2022,** 10 (3), 673–682.

(30) Konstantatos, G.; Sargent, E. H. PbS Colloidal Quantum Dot Photoconductive Photodetectors: Transport, Traps, and Gain. *Appl. Phys. Lett.* **2007**, *91* (17), 173505.

(31) Chu, A.; Gréboval, C.; Prado, Y.; Majjad, H.; Delerue, C.; Dayen, J.-F.; Vincent, G.; Lhuillier, E. Infrared Photoconduction at the Diffusion Length Limit in HgTe Nanocrystal Arrays. *Nat Commun* **2021**, *12* (1), 1794.

(32) Moghaddam, N.; Gréboval, C.; Qu, J.; Chu, A.; Rastogi, P.; Livache, C.; Khalili, A.; Xu, X. Z.; Baptiste, B.; Klotz, S.; Fishman, G.; Capitani, F.; Ithurria, S.; Sauvage, S.; Lhuillier, E. The Strong Confinement Regime in HgTe Two-Dimensional Nanoplatelets. *J. Phys. Chem. C* **2020**, *124* (42), 23460–23468.

(33) Liu, H.; Lhuillier, E.; Guyot-Sionnest, P. 1/f Noise in Semiconductor and Metal Nanocrystal Solids. *Journal of Applied Physics* **2014**, *115* (15), 154309.

(34) Lai, Y.; Li, H.; Kim, D. K.; Diroll, B. T.; Murray, C. B.; Kagan, C. R. Low-Frequency (1/f) Noise in Nanocrystal Field-Effect Transistors. *ACS Nano* **2014**, *8* (9), 9664–9672.

(35) Wang, Y.-Y.; Yuan, R.; Wang, S.; Wang, Z.; Jin, Q. Internal Electric Field Profiling of 2D P-N Junctions of Semiconductor Devices by 4D STEM and Dual Lens Electron Holography. *Microscopy Today* **2022**, *30* (1), 24–29.

(36) da Silva, B. C.; Sadre Momtaz, Z.; Monroy, E.; Okuno, H.; Rouviere, J.-L.; Cooper, D.; Den Hertog, M. I. Assessment of Active Dopants and p–n Junction Abruptness Using In Situ Biased 4D-STEM. *Nano Lett.* **2022**, *22* (23), 9544–9550.

(37) Ella, L.; Rozen, A.; Birkbeck, J.; Ben-Shalom, M.; Perello, D.; Zultak, J.; Taniguchi, T.; Watanabe, K.; Geim, A. K.; Ilani, S.; Sulpizio, J. A. Simultaneous Voltage and Current Density Imaging of Flowing Electrons in Two Dimensions. *Nat. Nanotechnol.* **2019**, *14* (5), 480–487.
(38) Hofmann, P. Accessing the Spectral Function of in Operando Devices by Angle-Resolved Photoemission Spectroscopy. *AVS Quantum Sci.* **2021**, *3* (2), 021101.
(39) Nenashev, A. V.; Jansson, F.; Baranovskii, S. D.; Österbacka, R.; Dvurechenskii, A. V.; Gebhard, F. Effect of Electric Field on Diffusion in Disordered Materials. I. One-Dimensional Hopping Transport. *Phys. Rev. B* **2010**, *81* (11), 115203.
(40) Nenashev, A. V.; Jansson, F.; Baranovskii, S. D.; Österbacka, R.; Dvurechenskii, A. V.; Gebhard, F. Effect of Electric Field on Diffusion in Disordered Materials. II. Two- and Three-Dimensional Hopping Transport. *Phys. Rev. B* **2010**, *81* (11), 115204.
(41) Richert, R.; Pautmeier, L.; Bässler, H. Diffusion and Drift of Charge Carriers in a Random Potential: Deviation from Einstein's Law. *Phys. Rev. Lett.* **1989**, *63* (5), 547–550.
(42) Arkhipov, V. I.; Bässler, H. A Model of Weak-Field Quasi-Equilibrium Hopping Transport in Disordered Materials. *Philosophical Magazine Letters* **1993**, *67* (5), 343–349.
(43) Xing, Y.; Yazdani, N.; Lin, W. M. M.; Yarema, M.; Zahn, R.; Wood, V. Effect of Positional Disorders on Charge Transport in Nanocrystal Quantum Dot Thin Films. *ACS Appl. Electron. Mater.* **2022**, *4* (2), 631–642.

TOC graphic

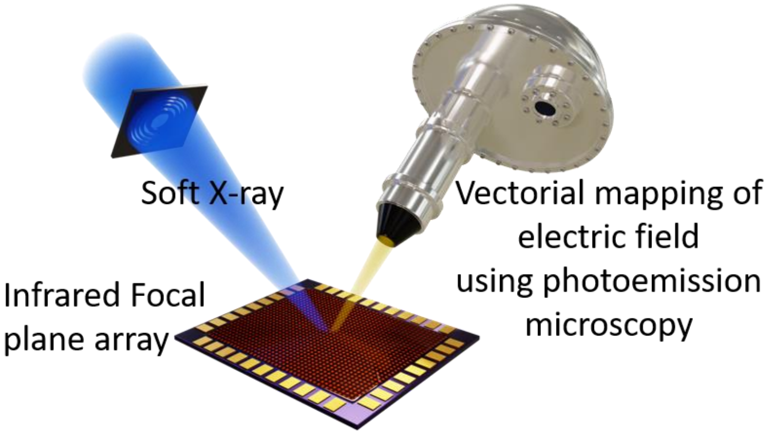
Soft X-ray
Vectorial mapping of electric field using photoemission microscopy
Infrared Focal plane array